applied sciences

MDPI

Article

Investigation on the Microstructural Diversity of a Three-Dimensional Porous Hydroxyapatite/Wollastonite Skeleton via Biomineralization in Simulated Body Fluids

Bin Jiang [1,2], Xin Li [3], Bozhi Yang [3], Shujie Yang [3], Xinyi Chen [3], Junhong Chen [1], Minghao Fang [3], Zhaohui Huang [3], Xin Min [3,*] and Xiaozhi Hu [1,*]

[1] School of Materials Science and Engineering, University of Science and Technology Beijing, Beijing 100083, China; jiangbin311@163.com (B.J.); chenjunhong2666@126.com (J.C.)
[2] School of Mechanical and Chemical Engineering, University of Western Australia, Perth, WA 6009, Australia
[3] School of Materials Science and Technology, China University of Geosciences (Beijing), Beijing 100083, China; lixincugb@foxmail.com (X.L.); yangbz98@163.com (B.Y.); yangshujie0903@163.com (S.Y.); chenxinyi521314@163.com (X.C.); fmh@cugb.edu.cn (M.F.); huang118@cugb.edu.cn (Z.H.)
* Correspondence: minx@cugb.edu.cn (X.M.); xiao.zhi.hu@uwa.edu.au (X.H.)

Abstract: The occurrence of fractures has emerged as one of the most prevalent injuries in the human body. In bone reconstruction surgery, after the implantation of porous hydroxyapatite materials, there is an initial infiltration of body fluids into the porous implant, followed by biomineralization-mediated apatite crystal formation and the subsequent ingrowth of bone cells. Despite extensive research efforts in this field, previous investigations have primarily focused on the formation of apatite crystals on exposed surfaces, with limited literature available regarding the formation of apatite crystals within the internal microstructures of bone implants. Herein, we demonstrate the occurrence of dynamic biomineralization within a three-dimensional porous hydroxyapatite/wollastonite (HA/WS) skeleton, leading to the abundant formation of nano-sized apatite crystals across diverse internal environments. Our findings reveal that these apatite nanocrystals demonstrate distinct rates of nucleation, packing densities, and crystal forms in comparison to those formed on the surface. Therefore, the objective of this study was to elucidate the temporal evolution of biomineralization processes by investigating the microstructures of nanocrystals on the internal surfaces of HA/WS three-dimensional porous materials at distinct stages of biomineralization and subsequently explore the biological activity exhibited by HA/WS when combined with cell investigation into apatite crystal biomineralization mechanisms at the nanoscale, aiming to comprehend natural bone formation processes and develop efficacious biomimetic implants for tissue engineering applications. The simultaneous examination of bone cell attachment and its interaction with ongoing internal nanocrystal formation will provide valuable insights for designing optimal scaffolds conducive to bone cell growth, which is imperative in tissue engineering endeavors.

Keywords: hydroxyapatite; biomineralization; apatite crystal; bone tissue

Citation: Jiang, B.; Li, X.; Yang, B.; Yang, S.; Chen, X.; Chen, J.; Fang, M.; Huang, Z.; Min, X.; Hu, X. Investigation on the Microstructural Diversity of a Three-Dimensional Porous Hydroxyapatite/Wollastonite Skeleton via Biomineralization in Simulated Body Fluids. *Appl. Sci.* **2023**, *13*, 11593. https://doi.org/10.3390/app132011593

Academic Editor: Nikolaos Kourkoumelis

Received: 22 September 2023
Revised: 20 October 2023
Accepted: 20 October 2023
Published: 23 October 2023

1. Introduction

With the advancement of medical technology, fractures have emerged as some of the most prevalent injuries in the human body. While external fixation techniques are suitable for stable fractures, patients with unstable fractures (such as comminuted fractures), advanced ages, abnormal bone metabolism, or osteoporosis exhibit a relatively increased risk of non-union or delayed union due to their limited fracture healing ability or compromised osteogenic capacity [1]. Consequently, bone reconstruction surgery utilizing artificial implant skeletons remains the primary treatment approach [2]. Currently, hydroxyapatite (HA) stands out as the most commonly employed biomaterial for fabricating these artificial implant skeletons. Following bone reconstruction surgery involving porous HA skeletons,

bodily fluids come into contact with and gradually infiltrate these structures, initiating biomineralization [3–6]. Apatite nanocrystals are slowly formed after the beginning of biomineralization. Due to the gradual infiltration of body fluids onto the porous HA skeleton, biomineralization occurs not only on the surface of the artificial porous HA skeleton but also, more importantly, inside the artificial porous HA skeleton [7–10]. In the later stage of the implantation of the artificial porous HA skeleton, bone cells grow onto the skeleton, and the microstructure of the skeleton plays an important role in the success of implantation. Therefore, this process will inevitably depend on the internal porous structure modification of the HA skeleton [11]. However, the apatite nanocrystals on the inner surface of the artificial porous HA skeleton are rarely studied, and their key role in bone growth and regeneration is unclear. Therefore, the study of the microstructure diversity of apatite nanocrystals formed by the biomineralization between the inner surface of the skeleton and body fluids and the influence of microstructure diversity on osteocyte adhesion play important roles in exploring the mechanism of bone growth and cell regeneration in an artificial porous skeleton [12–14].

At present, many studies [15–19] have investigated the biomineralization process of apatite nanocrystal formation in simulated body fluids (SBFs) and the related benefits of apatite nanocrystals in bone integration and regeneration. But, typically, such studies select fully exposed HA surfaces with non-porous characteristics, both experimentally and in modeling, to create controlled SBF contact environments. This is the most common way to study the basic principles of apatite crystal formation.

After bone reconstruction surgery, it is certain that the infiltration of the three-dimensional porous skeleton in body fluids is not synchronous [20]. The main reason is that the sizes, shapes, and surface texture states of the micro-channels, micro-pores, and micro-holes of the three-dimensional porous skeleton are different, so the microstructures of apatite nanocrystals formed by mineralization are diverse. Theoretically, different SBF contact environments lead to different types of nanocrystal structures that cannot be observed on HA surfaces soaked in a smooth, well-controlled SBF contact environment. Since the internal environment of the three-dimensional porous skeleton after undergoing biomineralization is more relevant to the growth of bone cells, the in-depth and detailed study of the unique nanocrystal structure "hidden" inside the three-dimensional porous skeleton will provide valuable insights into the nature of bone cell growth and bone tissue regeneration [20]. Although the study of micropores with different surface sizes (from a few μm to a few hundred μm) on the three-dimensional porous skeleton is important for the function of bone growth [21–24], it is equally important, or even more important, to study the biomineralization process and its microscopic diversity on the internal surface of the three-dimensional porous skeleton. Studies have shown that the internal micropore size and distribution of a three-dimensional porous skeleton have significant impacts on the early stage of bone integration [25–27]. In addition, recent studies have shown that the nucleation forms of apatite nanocrystals inside the three-dimensional porous skeleton are diversified during the stage of bone integration, which is mainly related to the contact environment between the skeleton and body fluids. Thus, it can be foreseen that the complex and constantly changing apatite nanocrystal structure in the three-dimensional porous skeleton structure is critical to the success of the skeleton at all stages of bone growth. Therefore, the purpose of this study was to reveal the change rule of the three-dimensional porous skeleton during the biomineralization process by studying the microstructures of the nanocrystals on the inner surface of a Hydroxyapatite/Wollastonite (HA/WS) three-dimensional porous skeleton at different biomineralization stages and to further study the biological activity of the three-dimensional porous HA/WS skeleton when it was simulated with in vitro cells. The adhesion of bone cells and the interaction of these cells with the ongoing formation of internal apatite nanocrystals were also studied. The results will give us clear indications for designing the ideal skeleton for bone cells, which is urgently needed for tissue engineering.

2. Materials and Methods

2.1. Materials

Hydroxyapatite was sourced from the Sigma-Aldrich (Shanghai, China) Trading Co., Ltd. Wollastonite came from Siyuan Mining (Xinyu, China) Co., Ltd. and polymethyl methacrylate (PMMA) and Gelatine were purchased from Aladdin Reagent (Shanghai, China) Co., Ltd. Deionized water was produced at our laboratory. NaCl, $NaHCO_3$, KCl, $Na_2HPO_4{\cdot}2H_2O$, $MgCl_2{\cdot}6H_2O$, Na_2SO_4, $CaCl_2{\cdot}H_2O$, Tris, and HCl were purchased from Aladdin Reagent (Shanghai, China) Co., Ltd.

2.2. Preparation of Three-Dimensional Porous HA/WS Skeleton and 1.5 × SBF

In this study, a three-dimensional porous HA/WS skeleton with random micropore structure was prepared by using freeze-drying method. The three-dimensional porous HA/WS skeleton was prepared by sintering 95 wt% HA and 5 wt% wollastonite at 1250 °C. Wollastonite was added because of its ability to form glass phase at high temperatures, thus providing additional mechanical strength to the three-dimensional porous skeleton. As is shown in Figure 1, the process involves these steps: Weigh 950 g of hydroxyapatite (HA) and 50 g of wollastonite (WS), mix thoroughly, then add 4000 mL of deionized water. Add 100 g of PMMA, 200 g of gelatin, 50 g of a water reducer, and 50 g of $Na_5P_3O_{10}$ accelerator. The homogenized solution is freeze-dried to create a porous structure under the following experimental conditions: −20 °C for 12 h, −40 °C for 4 h, with a vacuum degree at 89 μBar. Dry at room temperature for an additional twelve hours with a vacuum pressure set at 23 μBar. Once completely dried, remove the samples from the dryer and place them into a high-temperature furnace set to non-pressure sintering at 1250 °C for two hours. Finally, obtain three-dimensional porous HA/WS skeleton in Figure 1.

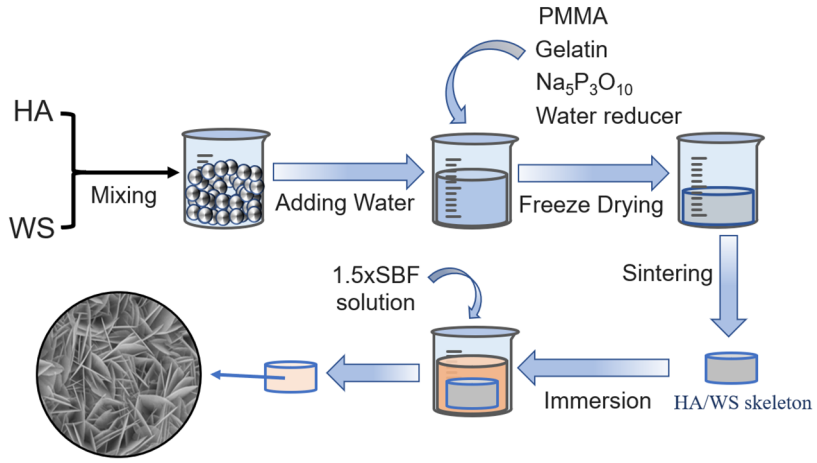

Figure 1. Schematic process for the preparation of a three-dimensional porous HA/WS skeleton and immersion in 1.5 × SBF solution.

Then, the prepared three-dimensional porous HA/WS skeleton was immersed in 1.5 × SBF solution for 3 weeks at a temperature of 37 ± 0.5 °C, with PH value maintained at 7.4, humidity controlled at 85%, and CO_2 concentration at 5%. After the immersion, the skeleton was removed from the 1.5 × SBF solution, washed with distilled water, and dried at room temperature. In order to observe the hidden apatite nanocrystals inside the three-dimensional porous HA/WS skeleton, the three-dimensional porous HA/WS skeleton was cut off and was sprayed with carbon layer on the exposed cross section for SEM observation.

2.3. Immersion of Three-Dimensional Porous HA/WS Skeleton in SBFs

In this study, 1.5 × SBF solution with ion concentration similar to that in human plasma was used. The solution contained analytical NaCl, $NaHCO_3$, KCl, $Na_2HPO_4{\cdot}2H_2O$,

$MgCl_2 \cdot 6H_2O$, Na_2SO_4, $CaCl_2 \cdot H_2O$, and tris. The prepared three-dimensional porous HA/WS skeleton was immersed in 1.5 × SBF solution for 3 weeks at a temperature of 37 ± 0.5 °C, with PH value maintained at 7.4, humidity controlled at 85%, and CO_2 concentration at 5%. After the immersion, the skeleton was removed from the 1.5 × SBF solution, washed with distilled water, and dried at room temperature. In order to observe the hidden apatite nanocrystals inside the three-dimensional porous HA/WS skeleton, the three-dimensional porous HA/WS skeleton was cut off and was sprayed with carbon layer on the exposed cross section for SEM observation.

2.4. Analysis Method

The microscopic morphology of three-dimensional porous HA/WS skeleton and cell adhesion status were observed using a field emission scanning electron microscope (SEM, model Zeiss-1555-VPFE-SEMe from Oberkochen). The microscopic diversity of apatite nanocrystals on biomineralized three-dimensional porous HA/WS skeleton was evaluated by using the different types of micro morphologies observed using scanning electron microscopy. The elements on the crystal surface were evaluated by using an energy dispersion spectrometer. The different microstructures of nanocrystals on HA/WS were observed using scanning electron microscope to evaluate the results of HA/WS after biomineralization. The adhesion status of osteoclasts on HA/WS samples after cell culture in vitro was observed with optical microscope (model BX53M from Olympus). Since HA/WS is a three-dimensional porous material, different from plate samples, the biological activity of osteoclasts on HA/WS can only be evaluated by observing the adhesion status and quantity distribution of osteoclasts on HA/WS using optical microscopy.

3. Results and Discussion

3.1. The Effect of SBF Immersion on the Microstructure of an HA/WS Skeleton

The microstructures of apatite nanocrystals "hidden" on the inner surface of the three-dimensional porous HA/WS skeleton during the inward growth of bone cells were investigated by using a high-intensity field emission scanning electron microscope (SEM). It has been shown that two different types of apatite nanocrystals are formed during the process of biomineralization and the inward growth of bone cells [15,28,29]. In this study, we observed two different types of apatite nanocrystals: one was a circular apatite nanocrystal, located on the surface of the sintered three-dimensional porous HA/WS skeleton, and the other was a sail-like nanocrystal cluster located on the top of the circular nanocrystal. The two main types of apatite nanocrystals can be observed from the oblique surface microstructure and in a cross-sectional view of the three-dimensional porous HA/WS skeleton, as shown in Figure 2a. The red and blue illustrations show two different types of apatite nanocrystals inside the three-dimensional porous HA/WS skeleton. The purpose of this study was to study the interior of the three-dimensional porous HA/WS skeleton to explore the microscopic diversity of apatite nanocrystals "hidden" in it and their influence on the adhesion of biological cells.

In this study, a three-dimensional porous HA/WS skeleton with a random micropore structure was prepared using the freeze-drying method [30–32]. In addition to the changes in the internal pore structure of the three-dimensional porous HA/WS skeleton, it is also necessary to consider three representative structures in the three-dimensional porous HA/WS skeleton. When the three-dimensional porous HA/WS skeleton and SBF come into contact, three different SBF contact environments are formed. The three SBF contact environments are shown in Figure 2b: (i) micropores fully filled with SBFs, (ii) half-full-with-SBF contact environments that exist due to the presence of partial air pressure in the pores or limited SBF infiltrate, and (iii) completely closed micropores, with only a wall or where just a limited SBF quantity infiltrates through micropore channels and adheres to the inner walls of the micropores. Detailed studies of apatite nanocrystals formed in these unique SBF contact environments will enable us to understand the internal microstructure

changes resulting from the formation of apatite nanocrystals to assess their potential impact on bone cell growth and bone tissue regeneration in future studies.

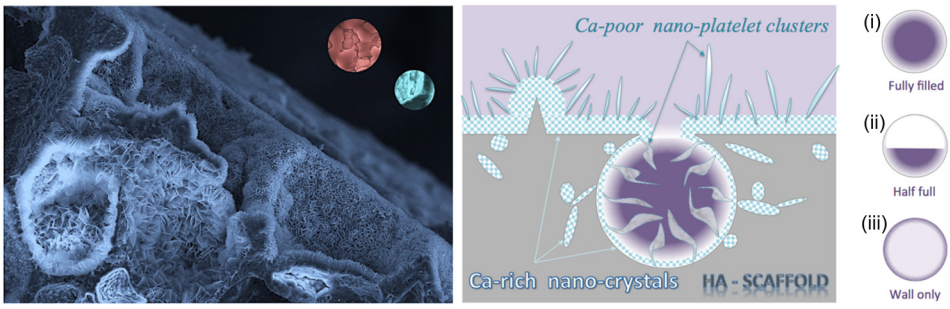

Figure 2. Microstructure of a nanocrystal. (**a**) Tilted landscape and near-surface cross-section view of the porous HA/WS skeleton. Red and blue insets stand for two different nanocrystal structures. (**b**) Three typical internal environments inside HA/WS skeleton: (**i**) fully filled by SBFs, (**ii**) half-full, (**iii**) wall-only (SBF is diffused through and attached only to the cavity wall).

Kim et al. [15] explained the formation process of apatite nanocrystals distributed on the surface after SBF contact with sintered HA. First, calcium ions of positive valence contact and react with the exposed HA surface to form calcium-rich apatite nanocrystals. Then, the calcium-rich nanocrystals contact and react with negative phosphate ions to form calcium-poor apatite nanocrystals. The alternating process and dynamics of crystal formation are affected by the total amount of positive calcium and the number of negative phosphate ions available for crystallization. If the total concentration of positive calcium ions and negative phosphate ions changes, different types of apatite nanocrystals will be formed. Therefore, according to the results of Kim et al., it can be concluded that in a settled concentration of SBFs, the general trend of forming apatite nanocrystals is that the calcium-rich apatite nanocrystals are located at or near the surface of sintered HA while the calcium-poor apatite nanocrystals are located away from the surface of sintered HA.

Figure 3a is the original electron microscope photograph with a scale of the three-dimensional porous HA/WS skeleton, showing the surface microstructure of the micro-holes inside the HA/WS skeleton. It can be seen from Figure 3a that there are completely closed holes and half-closed holes in the HA/WS skeleton. Figure 3b–d show a detailed enlarged image of Figure 3a. It can be seen that there are relatively dense apatite nanocrystal layers and sail-like apatite nanocrystals on the surface. According to the overall formation trend of calcium-rich apatite nanocrystals and calcium-poor apatite nanocrystals under quantitative SBF conditions, the relatively dense apatite crystal layer comprises the first calcium-rich apatite nanocrystals formed at the initial crystallization stage while the sail-like apatite nanocrystals are the calcium-poor apatite nanocrystals formed at the later crystallization stage.

As shown in Figure 3a–c, the SBF permeates the inner micropores, micro-channels, and micro-holes of the three-dimensional porous HA/WS skeleton surface and forms calcium-rich apatite nanocrystals. Due to the relatively abundant supply of calcium ions in the external body-fluid environment at the initial crystallization stage, calcium-rich apatite nanocrystals are formed. Moreover, these calcium-rich apatite nanocrystals gradually form a dense coating of apatite nanocrystals on the outer surface of the three-dimensional porous HA/WS skeleton. Holes with closed surfaces or small openings are less infiltrated by the SBF than holes with completely open or large openings, and so, the supply of calcium ions is limited, resulting in the formation of calcium-poor apatite nanocrystals. As shown in Figure 3a–c, since the outer surface of the three-dimensional porous HA/WS skeleton is in full contact with the SBF solution, more calcium ions are available for the formation of apatite nanocrystals, and so, a thicker and dense coating of calcium-rich apatite nanocrystals is formed on the outer surface of the three-dimensional porous HA/WS skeleton. As can be seen from Figure 3d, the dividing line between the HA/WS skeleton

and apatite nanocrystals is relatively obvious. Because of the different SBF environments, the different calcium ion concentrations, and the different micropore structures, different forms of apatite nanocrystals are formed inside and outside the three-dimensional porous HA/WS skeleton. It must be noted that the formation of the tunnel wall (about 8 μm thick) shown in Figure 3d has similar characteristics to the apatite film (about 500 nm) observed under TEM [33]. The results show that the concentration of calcium ions has a great influence on the type and thickness of apatite nanocrystal coating.

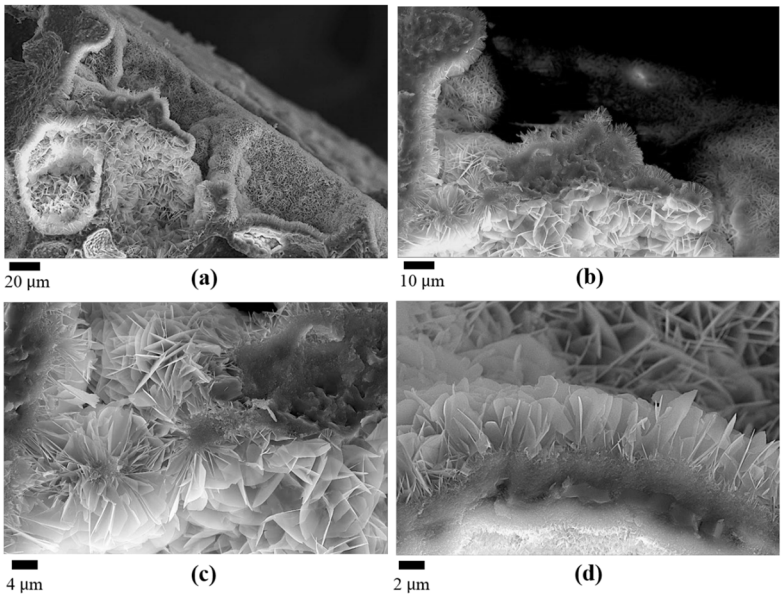

Figure 3. The complex microstructure of the three-dimensional porous HA/WS skeleton. (**a**) Completely closed and half-closed holes. (**b**) Enlarged view of the mid-section in (**a**), showing different interior sail-like nano-platelet clusters. (**c**) Enlarged view of (**b**), showing a small entry has been sealed by the nano-platelet crystal formations. (**d**) Enlarged view of an enclosed cavity at the bottom-right in (**a**).

Figure 4a is the microstructure picture of the outer surface of the three-dimensional porous HA/WS skeleton. It can be observed that the boundary between the mirror-like surface and the rough area is easily distinguished. The completely open micro-holes and micro-channels in the three-dimensional porous HA/WS skeleton and the pores near the surface are completely filled with apatite nanocrystals, and a dense apatite nanocrystal coating is formed on the surface of the HA/WS skeleton. This may have a significant impact on the role of micro-holes, micro-channels, and micropores in bone regeneration. In actual bone implantation surgery, whether to promote or restrict the growth of apatite nanocrystals depends on the reaction of the skeleton with bone cells. In part, this may explain why bone marrow cells and regenerative stem cells should be transplanted into the skeleton fold before actually being implanted [34–36].

Since the total time of SBF immersion was only three weeks, the experimental results show that the dense apatite nanocrystals coating of about 2 μm as shown in Figure 4b can be formed within 21 days and the deposition rate of apatite nanocrystals exceeds 100 nm per day. Due to the proven biomineralization process, the growth of apatite nanocrystals on the surface and internal micropores structures in weeks is critical for the success of artificial skeleton implantation. On the other hand, the results in Figure 4a show that the apatite nanocrystals formed during the immersion process with SBF can cover the holes and gaps, thus proving that the apatite nanocrystals formed by the biomineralization process of the HA/WS skeleton and SBF can repair micro-cracks in the natural HA system such as in the teeth and bones.

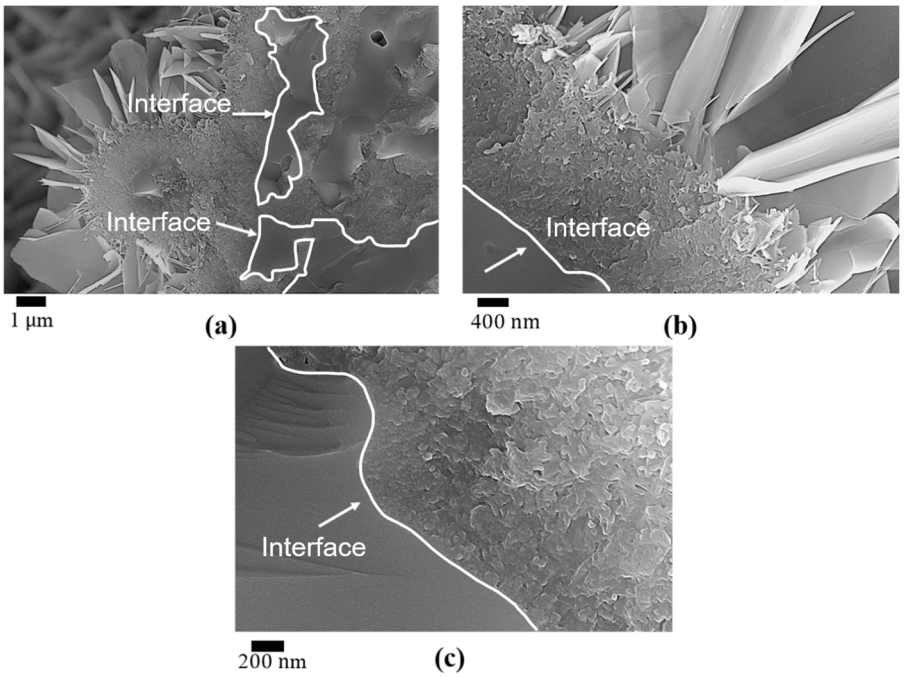

Figure 4. A crystal-clear view of the surface at nano-scale. (**a**) An HA/WS grain apex on the uneven skeleton surface. (**b**) The interface between HA/WS and apatite nanocrystals. (**c**) Enlarged view of (**b**). The extension of the interface in (**b**), showing a perfect interface at the nano-scale.

On the relatively uneven surface of the three-dimensional porous HA/WS skeleton (left of Figure 4a), the vertices of the HA/WS skeleton grains are surrounded by clusters of calcium-rich apatite nanocrystals and calcium-poor sail-like apatite nanocrystals. The combination of the two types of apatite nanocrystals effectively doubles the total thickness of the coating, which is advantageous if bone integration is a major consideration for a particular implant. Figure 4b,c show the interface between the HA/WS skeleton and the apatite nanocrystals; this may be the first time that the interface between the artificial skeleton and the apatite nanocrystals has been clearly observed using scanning electron microscopy, and this interface is perfect even at the nanoscale. In addition, the interface between the HA/WS skeleton and apatite nanocrystals shows no signs of cracking, indicating strong interface bonding. It can be seen from Figure 4c that the apatite nanocrystals at the interface are of the smallest size, which is only about 50 nm. As apatite nanocrystals grow outward gradually, the sizes and shapes of the apatite nanocrystals increase gradually. The disparity between Figures 4 and 5 illustrates the generation of distinct apatite nanocrystals on the external and internal surfaces of the exposed three-dimensional porous HA/WS skeleton.

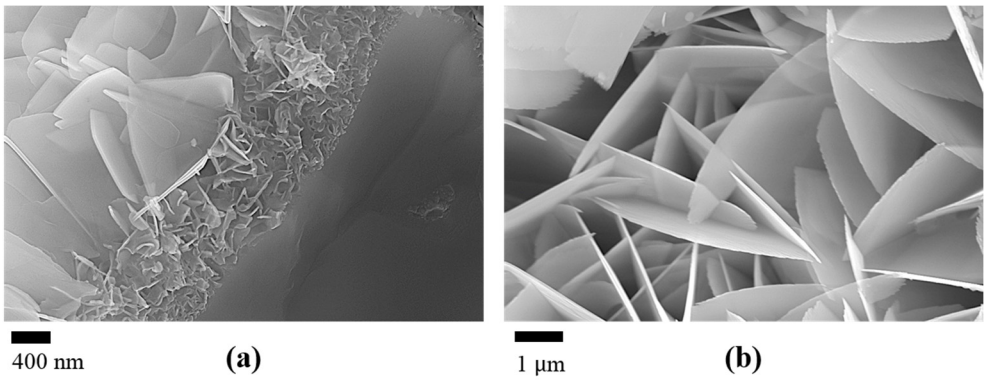

Figure 5. Nanocrystals close to the interface inside the scaffold. (**a**) Apatite nano-crystals formed on the HA. (**b**) Top view of sail-like nano-platelet clusters.

Figure 6 shows a natural cross-sectional view of the subtle changes in the microstructures of apatite nanocrystals in a half-full cavity. The relatively diluted SBF and limited calcium ions within this internal cavity facilitate the formation of apatite nanocrystals exclusively on the bottom surface of the groove, which is distinct from their absence on the three-dimensional fracture plane, as depicted in Figure 4 or Figure 5. Another obvious difference is that the apatite nanocrystals on the outer surface of the HA/WS skeleton are tightly arranged while the apatite nanocrystals in the inner half-full cavity are loosely arranged, as shown in Figure 6c. Therefore, the observations in Figures 5 and 6 are consistent, and they both reflect the influence of calcium ion concentration inside the HA/WS skeleton on the formation of apatite nanocrystals.

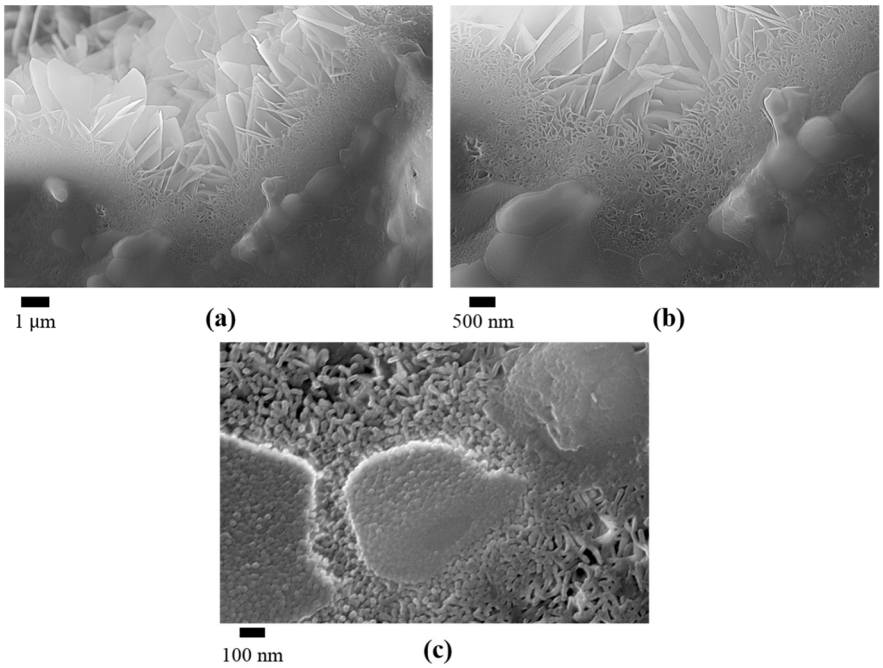

Figure 6. A microscopic view of the V-bottom interior of HA/WS skeleton. (**a**) Micrographs of the interior environment of the half-full cavity. (**b**) Enlarged view of the flat surface and the V-bottom section, showing seaweed-like nanocrystals. (**c**) Further enlarged view at the V-bottom.

The two distinct internal apatite nanocrystal structures depicted in Figure 7a,b were utilized in the illustration presented in Figure 2 to emphasize the objective of this study, which was to investigate the microstructural diversity of apatite nanocrystals within a three-dimensional porous HA/WS skeleton. In Figure 7a, a portion of the pure wall can be observed on the inner surface of the cavity. The occurrence of the pure wall phenomenon on the inner hole surface is attributed to the high concentration of wollastonite's glass phase, which is formed during the sintering process at elevated temperatures. The microstructure of the tiny caverns inside, as shown in Figure 7b, exhibits a more intricate composition, suggesting that the distinct microstructures of the apatite nanocrystals reflect variations in the SBF contact environment. The internal micropore structure of the bone implant skeleton may therefore require redesigning in accordance with the preferences of bone cells and bone regeneration. The internal micropore structure of an SBF needs to undergo in vitro cell tests after different periods of infiltration, highlighting the necessity of the careful tailoring of biomaterials with appropriate chemical composition, microstructure, pore size, and porosity to optimize conditions for stimulating bone tissue regeneration [37–40]. Engineered cells and gene-activated materials [41–44] will open up new avenues for research on bone growth and regeneration by incorporating bioabsorbable apatite nanocrystals with diverse micro morphologies into the three-dimensional micropore structure of the material.

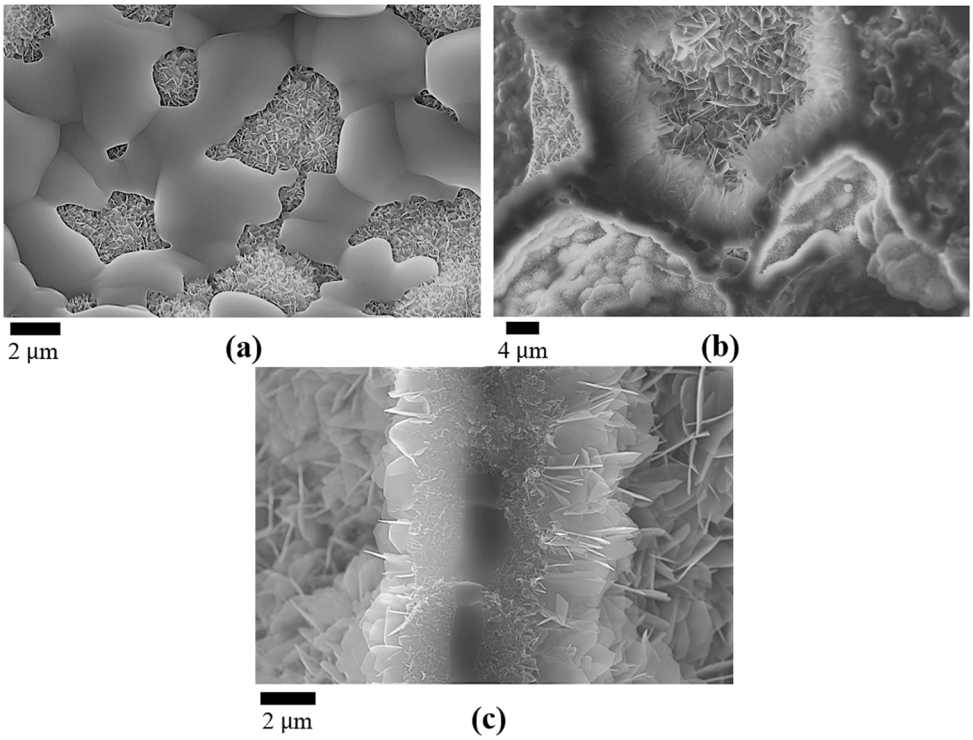

Figure 7. Diverse types of apatite nanocrystals. (**a**) The cavity wall is covered mostly by the impermeable glass phase of wollastonite. (**b**) Miniature caves with different SBF contact conditions. (**c**) Thin wall between two fully filled cavities.

Figure 7c illustrates the presence of a narrow wall, measuring approximately 1 μm, separating the two fully occupied internal micro-caves. The micropores in the cavity wall were filled with calcium-rich apatite nanocrystals, which subsequently formed a compact coating of approximately 1 μm thick apatite nanocrystals on both sides. The presence of clusters consisting of calcium-deficient apatite nanocrystals on both sides indicates the closure of pre-existing micro-holes in the thin wall by these nanocrystals, suggesting a modification in the opening system within the skeleton. Consequently, further research is required to optimize skeleton design considering fluid infiltration and apatite nanocrystal formation, enabling the efficient utilization of cells and genes for activating apatite crystal formation while minimizing potential adverse side effects on the open-hole skeleton system.

The internal environment of the sintered three-dimensional porous HA/WS skeleton is significantly more intricate compared to the flat and fully exposed surface utilized in current biomineralization studies [8,28,29,45]. In addition to the large open micropores ranging from 50 μm to 500 μm in size, there exist numerous micropores and nanopores on the inner wall, which are interconnected through various means. The formation conditions of apatite nanocrystals in three distinct SBF contact environments, as depicted in Figure 2b, further contribute to the intricate nature of the structure. The observations demonstrate that the inherent variations in internal conditions inevitably give rise to the heterogeneity of apatite nanocrystals. The crystallization process, even when constrained by a specific and well-defined condition such as the internal angle or nanoscale surface roughness, continues to present novel discoveries and challenges. The key functions of the apatite nanocrystal structure in the three-dimensional porous skeleton need to be investigated from various perspectives including crystal engineering [46–48] and tissue engineering [49–54].

A three-dimensional structural image of the skeleton was acquired using a micro-computed tomography (Micro-CT) system, specifically the Skyscan 1176 Micro-CT, provided by the Harry Perkins Medical Center at Xihua University. The macroscopic morphology and interconnected pore structure of the sintered three-dimensional porous HA/WS skeleton obtained using Micro-CT are illustrated in Figure 8. The Micro-CT analysis reveals

that both freeze-drying and non-pressure sintering methods yield a characteristic three-dimensional porous HA/WS skeleton with an interconnected pore structure extending from the external to the internal regions, exhibiting a diverse distribution of pore sizes ranging from approximately 100 to 500 μm. The interconnected porous structure and high porosity of the three-dimensional HA/WS skeleton provide an optimal environment for cellular cultivation, proliferation, and tissue growth.

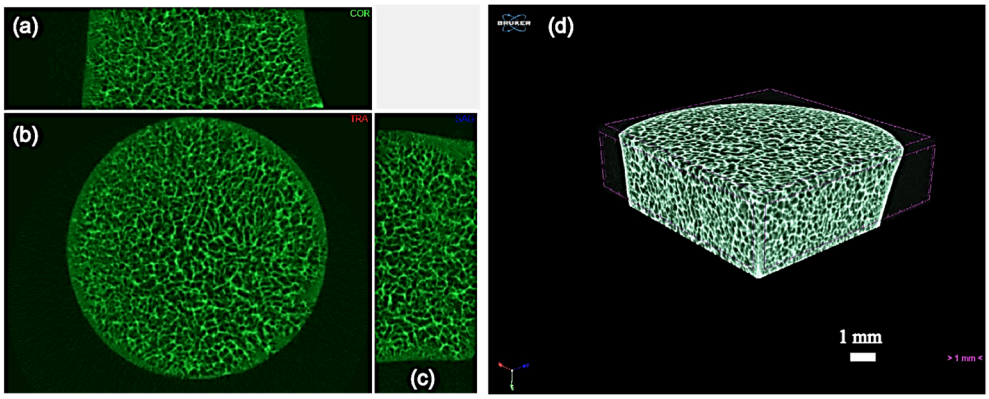

Figure 8. Morphology of the 90HA/10WS scaffolds obtained via micro-CT analysis. (**a**) Front view; (**b**) top view; (**c**) side view; and (**d**) inside cutting-surface view.

The results demonstrate the occurrence of active biomineralization processes within the three-dimensional porous HA/WS skeleton, revealing nanoscale microstructure details of the inner surface that are seldom observed on the exposed outer surface. In a clinical context, it is anticipated that the internal pore structure and morphology of bone implants will gradually evolve due to the formation of ever-changing apatite nanocrystals during biomineralization. This suggests that conducting bone cell experiments on skeletons with an internal porous structure at different time points after SBF infiltration will provide further insights into the effects of bone cell and bone tissue regeneration. In vitro cell culture tests should be performed on the internal structure of the three-dimensional porous HA/WS skeleton exposed after SBF infiltration, which will determine how these hidden internal apatite nanocrystals interact with bone cells and thus determine the bone regeneration process. Therefore, it is crucial to pay close attention to relevant SBF simulations and in vitro cell experiments. To our knowledge, this aspect has not been systematically investigated.

3.2. The Effect of SBF Immersion Time on the Microstructure of the HA/WS Skeleton

The morphological comparison of the three-dimensional porous HA/WS skeleton before and after immersion in SBF solution is illustrated in Figure 9. The surface of the three-dimensional porous HA/WS skeleton exhibited a relatively dense biomineralized layer after being immersed in 1.5 × SBF for 21 days, as depicted in Figures 5–9. After conducting further observations of the local area, it was discovered that the generated apatite exhibited a thin sheet structure, and this formation was found to be closely associated with the crystallographic characteristics and orientation of apatite crystals. The sheet has a diameter of approximately 2 μm, with a thickness ranging in the dozens of nm. It is intricately interwoven and intertwined. The deposition of hydroxyapatite in simulated body fluids within the HA/WS three-dimensional porous skeleton can be observed in Figure 9, demonstrating a three-dimensional directional growth. Furthermore, the biological mineralization process leads to the formation of apatite nanoparticle crystals within the cavities, walls, and inner surfaces of the three-dimensional porous HA/WS skeleton.

The biomineralization process being dynamic in nature, the osmosis gradually progresses inward as the simulated body fluid comes into contact with the three-dimensional porous HA/WS skeleton and the infiltration time increases. The internal cavity structure becomes intricate due to variations in the SBF contact environment. As immersion progresses, the biomineralization process differs across these environments, resulting in the

formation of distinct types of apatite nanocrystals during mineralization. The internal micropore structure of the implant skeleton may require redesigning based on bone cell preferences and regeneration needs. Therefore, it is necessary to investigate the changes in the internal micropore structure after different durations of SBF soaking. In this study, a three-dimensional porous HA/WS skeleton was immersed in 1.5 × SBF solution for varying periods (1 day, 3 days, 7 days, 14 days, and 21 days) under identical culture conditions. After each immersion period, excess impurities were removed from the surface via cleaning with deionized water followed by drying at room temperature. The effect of simulated body fluid immersion time on the microstructure of the three-dimensional porous HA/WS skeleton was observed using scanning electron microscopy.

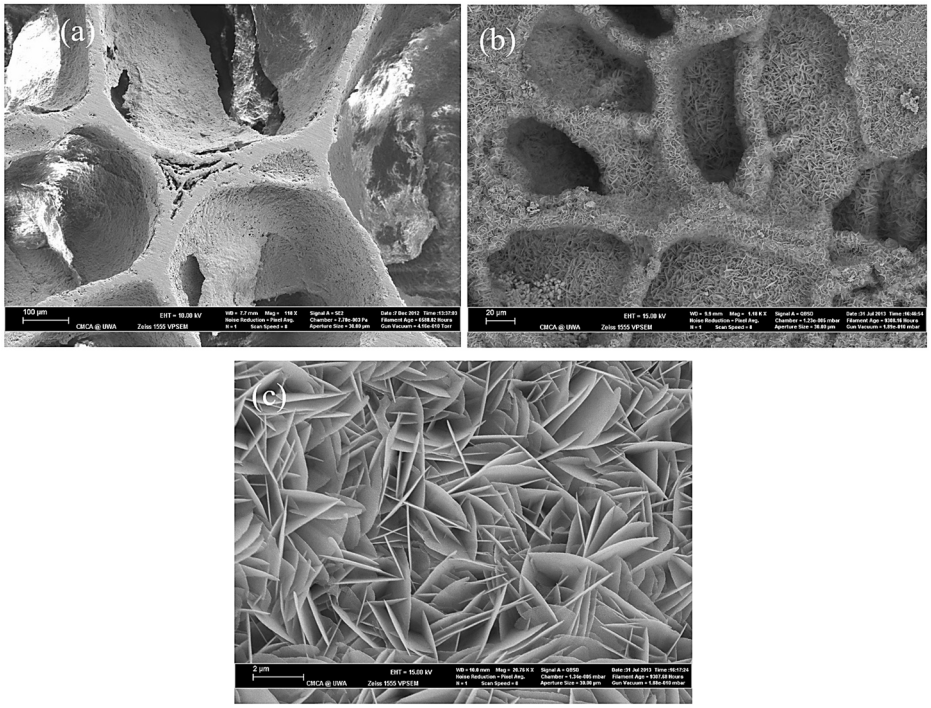

Figure 9. (**a**) Microstructure of three-dimensional porous HA/WS skeleton before immersion; (**b**,**c**) microstructure of three-dimensional porous HA/WS skeleton after 21-days immersion.

The microstructure of the three-dimensional porous HA/WS skeleton after being immersed in simulated body fluids for 1 day is depicted in Figure 10. The observation from Figure 10a reveals that following a 1-day immersion period, only a few apatite nanocrystals grow on the three-dimensional porous HA/WS skeleton surface within certain grooves. This can primarily be attributed to the short duration of immersion, which corresponds to an early stage in the biomineralization process and consequently results in a slow crystal growth rate. Upon further certification (Figure 10b), a lake-like distribution of apatite nanocrystals surrounded by a WS glass phase becomes apparent. The smooth region surrounding it represents the high-temperature-formed glass phase composed of WS while the area consisting of the central nanocrystal sheet signifies the cluster of apatite nanosheets formed through biomineralization. The subsequent magnification of the three-dimensional porous HA/WS skeleton surface provides clearer evidence that solely formed apatite nanocrystals are distributed within fluted areas. Based on experimental findings, it can be concluded that under a 1-day immersion time, there is a greater inclination for apatite nanoparticles to form within grooves present on the three-dimensional porous HA/WS skeleton surface.

The microstructure of the three-dimensional porous HA/WS skeleton after being soaked in simulated body fluids for 3 days is shown in Figure 11. It can be observed from Figure 11a that with an increased mineralization time, apatite nanocrystals are almost completely covering the surface of the three-dimensional porous HA/WS skeleton. The

distribution appears to be relatively uniform, and the stacked layers of nanosheets are relatively thin. Compared to an immersion time of 1 day, a more uniform distribution of apatite nanocrystals is evident after 3 days of immersion, indicating a relatively complete biomineralization process. Therefore, a relatively uniform layer of apatite nanocrystals can be formed on the surface of the three-dimensional porous HA/WS skeleton after a soaking time of 3 days.

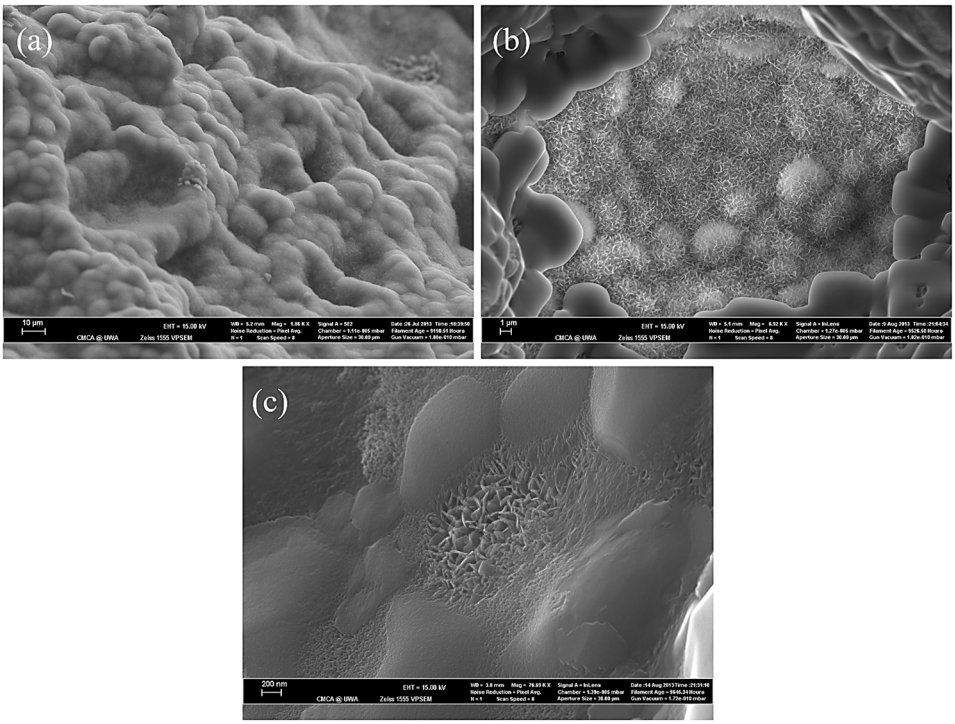

Figure 10. Microstructure of three-dimensional porous HA/WS skeleton immersed in simulated body fluids for 1 day. (**a**–**c**) SEM images of HA/WS skeleton after immersed in simulated body fluids for 1 day at different magnifications.

The microstructure of the three-dimensional porous HA/WS skeleton after 7 days of immersion in simulated body fluids is presented in Figure 12. It can be observed that mineralization is relatively complete with prolonged immersion time. The surface of the three-dimensional porous HA/WS skeleton is fully covered by apatite nanocrystals, which exhibit longitudinal growth and gradually accumulate on the original crystal layer. Furthermore, after 7 days of immersion, there is an evident increase in both length and thickness in the apatite nanocrystals on the surface of the three-dimensional porous HA/WS skeleton.

The microstructure of the three-dimensional porous HA/WS skeleton, as depicted in Figure 13, exhibits complete biomineralization after being immersed in simulated body fluids for a duration of 14 days. Notably, apatite nanocrystal sheets have effectively bridged the gap between the two cavities while a substantial coating of apatite nanocrystals has formed along the cavity wall.

The microstructure of the three-dimensional porous HA/WS skeleton after 21 days of immersion in simulated body fluids is presented in Figure 14. Prolonged immersing in simulated body fluids results in the formation of a relatively dense apatite nanocrystal coating on the surface of the three-dimensional porous HA/WS skeleton. With longer immersing durations, there is a gradual accumulation of mineralization, an interweaving of formed nanosheets, and even fusion in certain areas, resulting in a denser surface. In summary, increasing the duration of immersion in simulated body fluids gradually enhances the density and thickness of the crystal layer on the surface of the three-dimensional porous HA/WS skeleton. This confirms successful biological mineralization after culturing the three-dimensional porous HA/WS skeleton within a simulated human body

fluid environment, which promotes its biocompatibility within the human body. These findings contribute to understanding key functions played by apatite nanocrystals within three-dimensional porous HA/WS skeletons during bone regeneration.

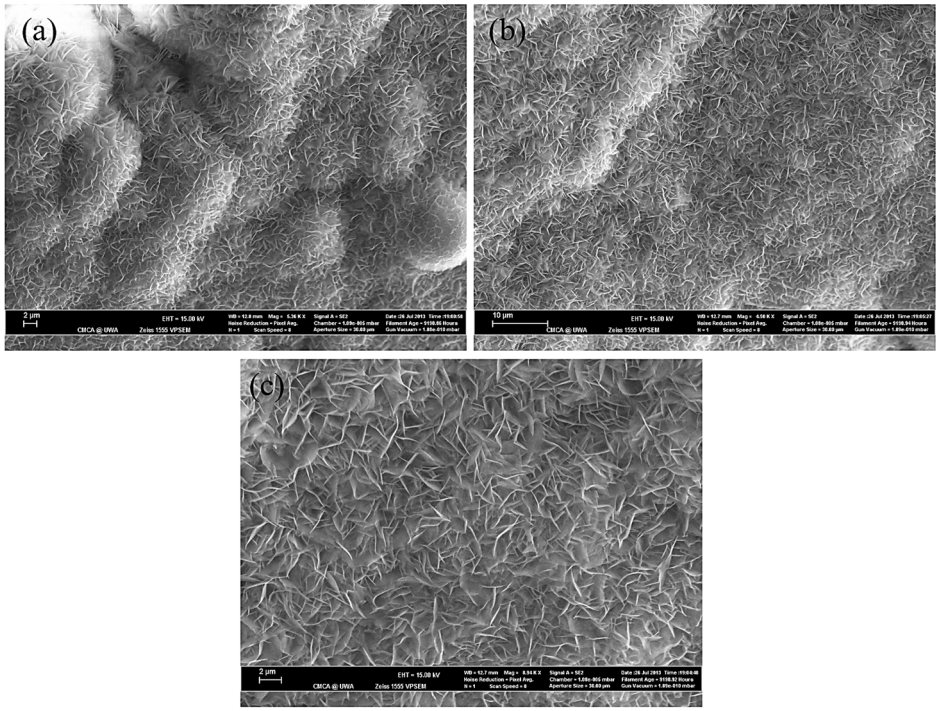

Figure 11. Microstructure of three-dimensional porous HA/WS skeleton immersed in simulated body fluids for 3 days. (**a**–**c**) SEM images of HA/WS skeleton after immersed in simulated body fluids for 3 days at different magnifications.

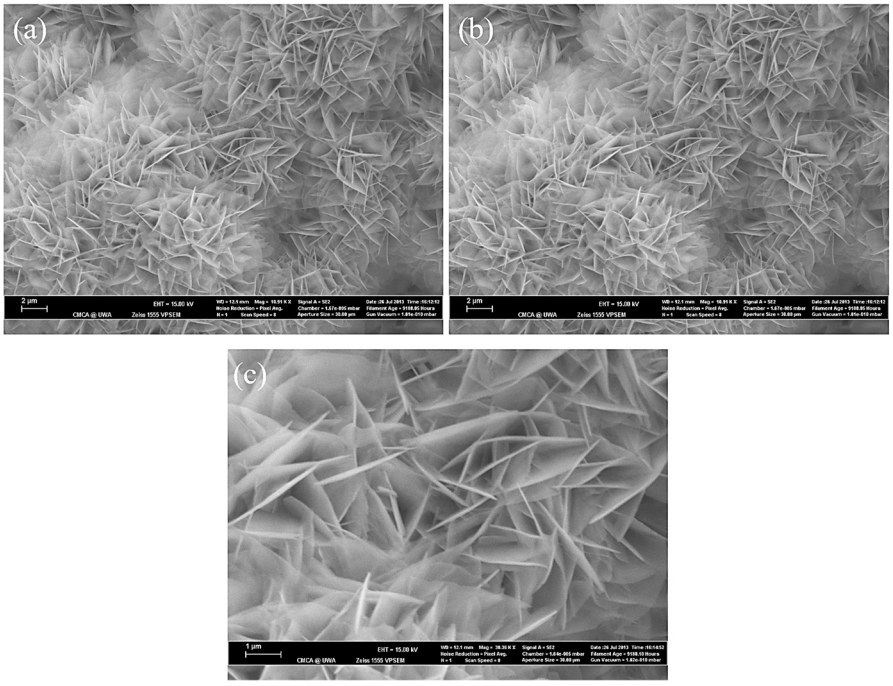

Figure 12. Microstructure of three-dimensional porous HA/WS skeleton immersed in simulated body fluids for 7 days. (**a**–**c**) SEM images of HA/WS skeleton after immersed in simulated body fluids for 7 days at different magnifications.

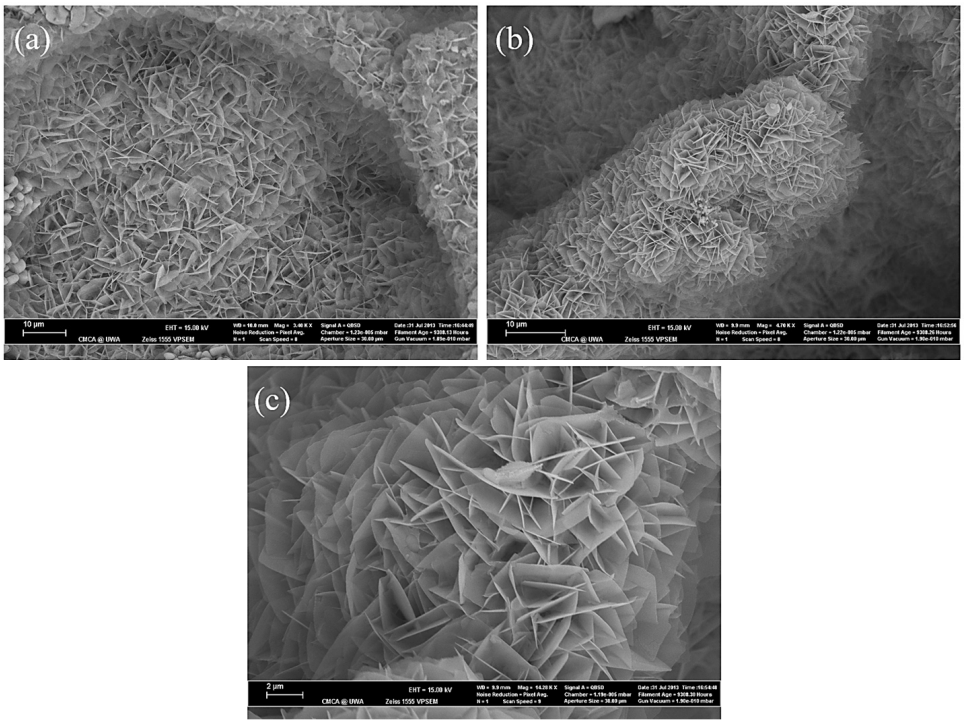

Figure 13. Microstructure of three-dimensional porous HA/WS skeleton immersed in simulated body fluids for 14 days. (**a**–**c**) SEM images of HA/WS skeleton after immersed in simulated body fluids for 14 days at different magnifications.

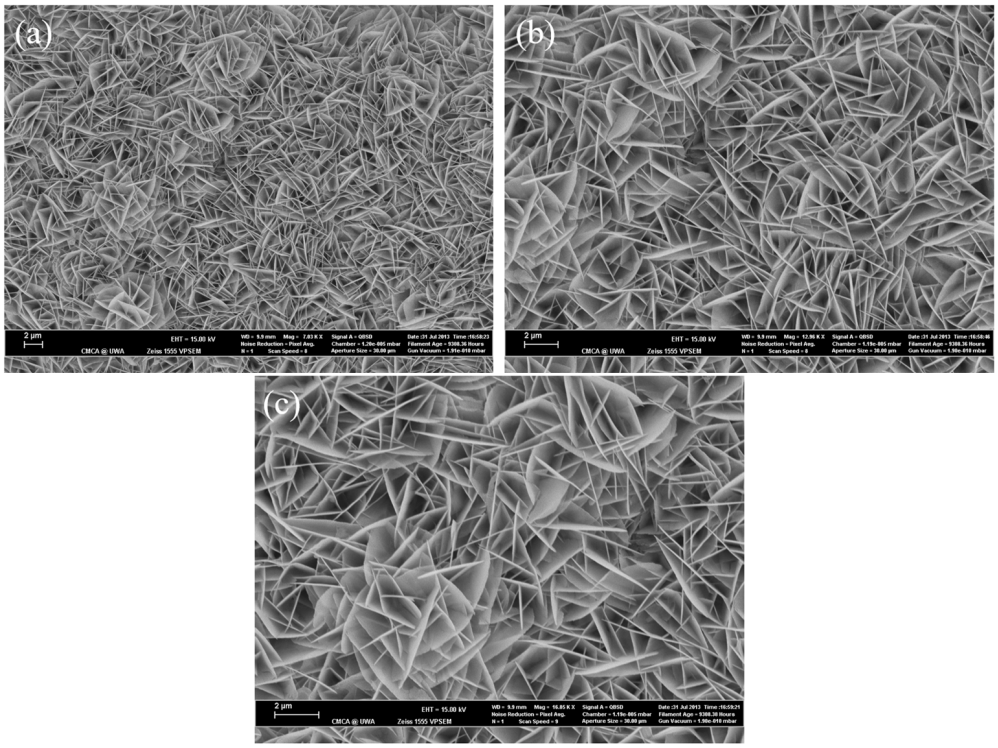

Figure 14. Microstructure of three-dimensional porous HA/WS skeleton immersed in simulated body fluids for 21 days. (**a**–**c**) SEM images of HA/WS skeleton after immersed in simulated body fluids for 21 days at different magnifications.

3.3. The Influence of SBF Immersion Time on the Surface Energy Spectrum of an HA/WS Skeleton

Energy dispersive spectroscopy (EDS) is a crucial technique for micro component analysis, enabling the simultaneous characterization of sample surface morphology and composition when combined with the SEM method. As depicted in Figure 15, calcium (Ca) elements are highlighted in red and phosphorus (P) elements in green during energy spectrum analysis. A substantial deposition of calcium and phosphorus elements from simulated body fluids onto the three-dimensional porous HA/WS skeleton surface was observed, without any noticeable accumulation. The distribution of elements provides an enhanced visualization of the morphology of laminar sediments, and an increase in immersion time in simulated body fluids leads to the formation of intensified biomineralization deposits. Based on EDS results, the sediments primarily consist of calcium and phosphorus minerals, with the released calcium and phosphorus from mechanical degradation being fully utilized during the mineralization process. Furthermore, the sediments were subjected to elemental quantitative analysis using the EDS electron probe. The results revealed the presence of Ca, P, and O elements in addition to C elements on the sediment surface. The results detailing the HA/WS surface element content after EDS analysis are shown. As illustrated in Figure 16, the EDS analysis of the prepared three-dimensional porous HA/WS skeleton revealed that the calcium content in the calcium-rich region was 32.6 atomic percent (At%) while the phosphorus content was 17.9 At%, resulting in a Ca/P ratio of 1.82. In contrast, the calcium content, phosphorus content, and Ca/P ratio were found to be 16.9 At%, 13.2 At%, and 1.28, respectively in the calcium-poor region. These experimental findings provide strong evidence supporting the crystal theory of calcium-rich and calcium-poor apatite discussed in this manuscript.

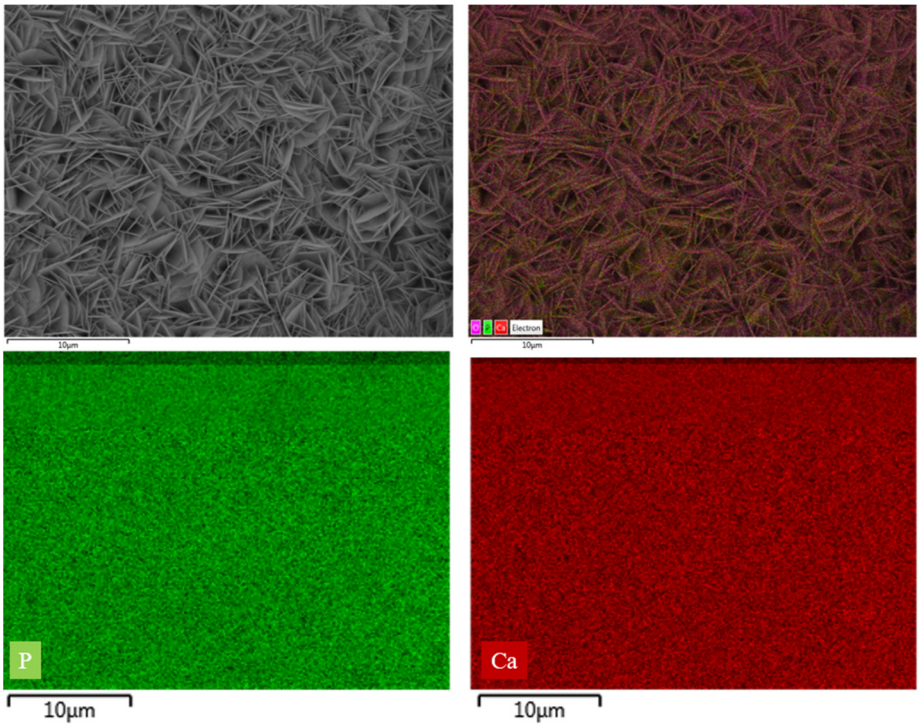

Figure 15. Surface morphology and elemental analysis of three-dimensional porous HA/WS skeleton immersed in simulated body fluids for 21 days.

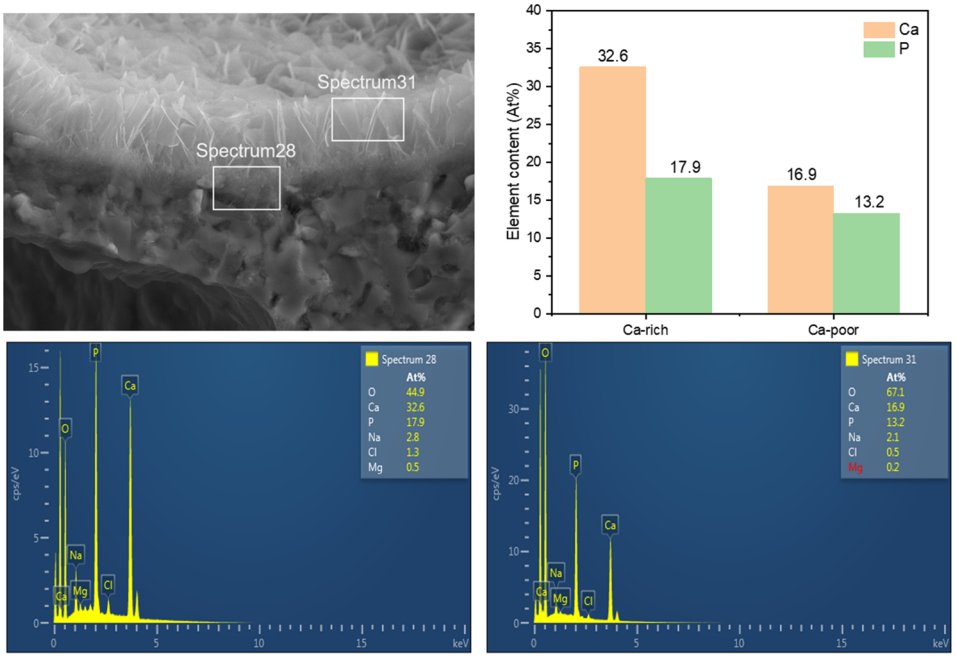

Figure 16. Surface element analysis results of three-dimensional porous HA/WS skeleton immersed in simulated body fluids for 21 days.

3.4. Experimental Study on Cell Adhesion within HA/WS Skeleton In Vitro

The C57BL/J6 murine preosteoclast cells were utilized for conducting in vitro cell adhesion assays on a three-dimensional porous HA/WS scaffold. The cells were seeded onto the scaffold, stimulated with 100 ng/mL rRANKL and 10 ng/mL M-CSF, and subsequently cultured under controlled humidified conditions. After three days of incubation, the cells were fixed using 4% PFA and lightly coated with carbon. The adhesion of cells to the porous skeleton was examined using both scanning electron microscopy as well as optical microscopy. Numerous researchers have acknowledged the extensive interactions between cells and the microenvironment surrounding the skeletal surface during in vitro growth and culture, with three-dimensional culture models being more adept at simulating in vivo conditions compared to traditional two-dimensional cell culture models. In order to construct a three-dimensional cell culture model, we devised and manufactured an HA/WS porous skeleton featuring an interconnected micro-scale porous network that facilitates fluid delivery through its pores, thereby closely mimicking natural cellular growth processes.

As depicted in Figure 17, osteoclasts exhibit robust adhesion, spreading, and proliferation on the three-dimensional porous HA/WS skeleton, indicating excellent biocompatibility. The presence of a three-dimensional porous structure further enhances the microenvironment for osteoclast adhesion and proliferation. Immersion in SBFs and the subsequent functional modification of the three-dimensional porous HA/WS skeleton to induce apatite nanocrystal formation within its structure represent an effective approach for promoting osteoclast adhesion, growth, and culture.

As depicted in Figure 18, the adhesion morphology of osteoclasts on the three-dimensional porous HA/WS skeleton was suboptimal in the absence of SBF immersion, with a sparse and uneven distribution. Only a limited number of osteoclasts exhibited adherence to the three-dimensional porous HA/WS skeleton. Despite imperfect adhesion, this observation still suggests that HA/WS three-dimensional porous skeletons possess biological activity.

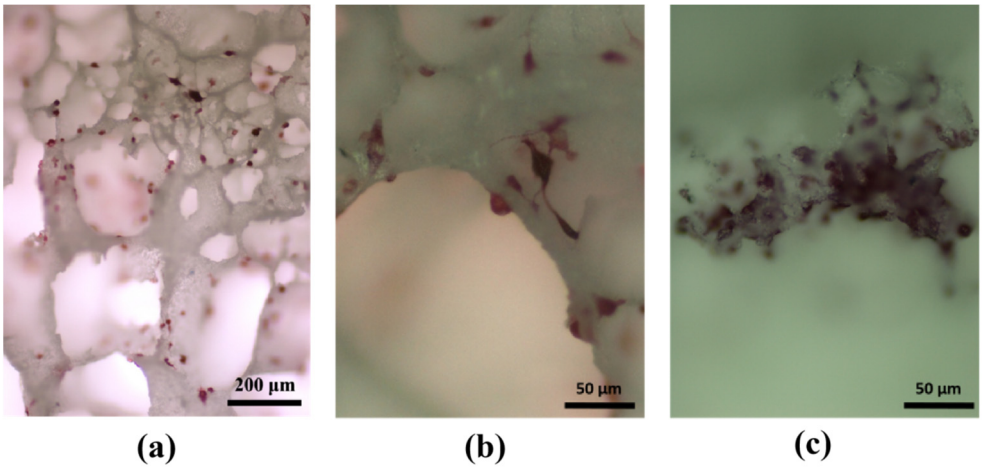

Figure 17. Optical images of adhesion status of osteoclast cell adhesion on HA/WS skeleton (top view) after 3 days of seeding; (**a**,**b**) non-SBF-immersed porous HA/WS skeleton; (**c**) SBF-immersed porous HA/WS skeleton.

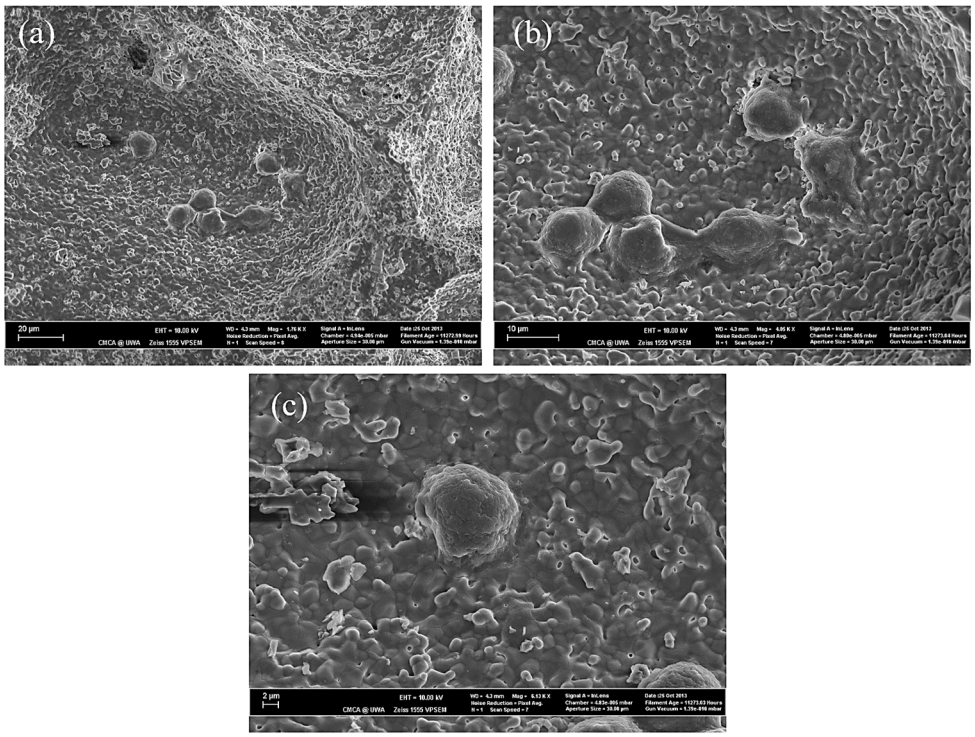

Figure 18. The SEM images of HA/WS three-dimensional porous osteoclasts cultured without SBF immersion. (**a**–**c**) SEM images of osteoclasts on HA/WS at different magnifications.

Comparing the three-dimensional porous HA/WS skeleton without SBFs, shown in Figure 18, and the three-dimensional porous HA/WS skeleton immersed in SBFs, shown in Figure 18c, the pretreatment of the three-dimensional porous HA/WS skeleton with SBF facilitated enhanced growth, permeation, and filling by osteoclasts. As shown in Figure 19, after SBF immersion, the proliferation of osteoclasts in the skeletal pore wall and inner pore was significantly promoted with the assistance of apatite nanocrystals. The results indicated that HA/WS three-dimensional porous skeleton had good biocompatibility, and the three-dimensional porous skeleton structure provided a good microenvironment for the adhesion and proliferation of osteoclasts, and promoted the adhesion, growth and culture of osteoclasts.

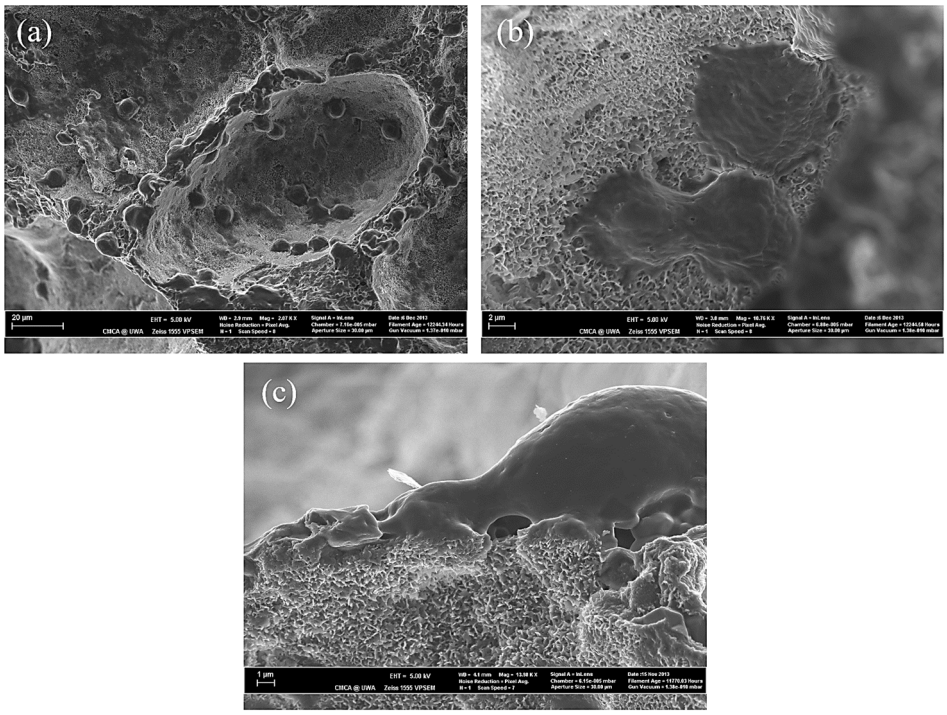

Figure 19. SEM images showing more details of osteoclast cell antenna adhesion on apatite nanocrystals of porous three-dimensional HA/WS skeleton. (**a**–**c**) Different views of cells attached tightly on walls and holes inside, at different magnifications, after 3 days of seeding.

The three-dimensional porous HA/WS skeleton possesses a highly porous network with an optimal pore size range of 100 μm to 500 μm, facilitating the fluid flow of SBFs in three-dimensional cell culture models. Our findings demonstrate that the pretreated apatite nanocrystal-coated three-dimensional porous HA/WS skeleton promotes the adhesion and proliferation of preosteoclast cells, making it more suitable for osteoclast culture compared to the surface of a conventional 24-well cell culture plate. Therefore, these innovative biomimetic three-dimensional porous HA/WS skeletons pave the way for potential clinical applications in growing autologous osteoclasts using in vitro three-dimensional cell culture models.

The three-dimensional porous HA/WS skeleton can also serve as a ceramic/polymer composite scaffold for interfacing bone and soft tissue, facilitating the reconstruction and regeneration of biological tissues. Moreover, it holds potential as a tissue engineering scaffold suitable for low-load applications such as cancellous bone replacement repair.

4. Conclusions

In this study, a three-dimensional porous HA/WS skeleton was incorporated into simulated body fluids to investigate the process of apatite nanocrystal formation through biomineralization and its microstructural diversity. Furthermore, mouse C57BL/J6 preosteoclast cells were employed for in vitro cell adhesion experiments. We observed the adherence of C57BL/J6 osteoclasts to the three-dimensional porous HA/WS skeleton and explored the influence of biomineralization-induced microstructure variations in apatite nanocrystals on cell adhesion, leading to the following conclusions:

(1) The biomineralization process was successfully achieved after a 21 day immersion in 1.5 × SBF, resulting in the formation of densely laminar apatite nanocrystals. These flake-shaped nanocrystals were deposited within the three-dimensional porous HA/WS skeleton pores, each with an outer diameter of approximately 2 μm, an inner layer thickness of about 1 μm, and a single thickness ranging in tens of nanometers. This morphology is attributed to the concentration and distribution of Ca ions present in simulated body fluids.

(2) Apatite nanocrystals exhibit exceptional interfacial properties with a three-dimensional porous HA/WS skeleton substrate. The sedimentary environment within the three-dimensional porous HA/WS skeleton is complex and diverse, resulting in diverse apatite nanocrystals being formed through biomineralization in SBF solution. These nanocrystals can enhance pore wall thickness, reduce original pore size, and promote densification. This highlights the practical significance of channel structure design in bio-porous materials. Furthermore, variations in microscopic morphology and particle size in apatite nanocrystals also significantly impact subsequent cell experiments.

Author Contributions: Conceptualization, B.J. and X.H.; methodology, M.F.; software, X.L.; validation, B.J., B.Y. and S.Y.; formal analysis, X.C.; investigation, X.M.; resources, X.H.; data curation, Z.H.; writing—original draft preparation, X.H.; writing—review and editing, B.J.; visualization, J.C.; supervision, Z.H.; project administration, X.M.; funding acquisition, M.F. All authors have read and agreed to the published version of the manuscript.

Funding: This research was funded by the Australian Research Council (ARC) Discovery Project Scheme, grant number DP110105296.

Institutional Review Board Statement: Not applicable.

Informed Consent Statement: Not applicable.

Data Availability Statement: Not applicable.

Conflicts of Interest: The authors declare that there are no conflict of interest regarding the publication of this paper.

References

1. Tan, W.; Gao, C.; Feng, P.; Liu, Q.; Liu, C.; Wang, Z.; Deng, Y.; Shuai, C. Dual-functional scaffolds of poly (L-lactic acid)/nanohydroxyapatite encapsulated with metformin: Simultaneous enhancement of bone repair and bone tumor inhibition. *Mater. Sci. Eng. C* **2021**, *120*, 111592. [CrossRef] [PubMed]
2. Wang, S.; Yang, Y.; Zhao, Z.; Wang, X.; Mikos, A.G.; Qiu, Z.; Song, T.; Sun, X.; Zhao, L.; Zhang, C. Mineralized collagen-based composite bone materials for cranial bone regeneration in developing sheep. *ACS Biomater. Sci. Eng.* **2017**, *3*, 1092–1099. [CrossRef] [PubMed]
3. Mancinelli, R.; Di Filippo, E.S.; Tumedei, M.; Marrone, M.; Fontana, A.; Ettorre, V.; Giordani, S.; Baldrighi, M.; Iezzi, G.; Piattelli, A. Human dental pulp stem cell osteogenic differentiation seeded on equine bone block with graphene and melatonin. *Appl. Sci.* **2021**, *11*, 3218. [CrossRef]
4. Boschetto, F.; Ngoc Doan, H.; Phong Vo, P.; Zanocco, M.; Zhu, W.; Sakai, W.; Adachi, T.; Ohgitani, E.; Tsutsumi, N.; Mazda, O. Antibacterial and osteoconductive effects of chitosan/polyethylene oxide (PEO)/bioactive glass nanofibers for orthopedic applications. *Appl. Sci.* **2020**, *10*, 2360. [CrossRef]
5. Bueno, C.R.E.; Sarmiento, J.L.; Vasques, A.M.V.; da Silva, A.C.R.; Cintra, L.T.A.; Santos, J.M.M.; Dezan-Júnior, E. Biocompatibility, Biomineralization and Induction of Collagen Maturation with the Use of Calcium Hydroxide and Iodoform Intracanal Dressing. *J. Funct. Biomater.* **2023**, *14*, 507. [CrossRef]
6. Chen, J.; Xing, Y.; Bai, X.; Xue, M.; Shi, Q.; Li, B. Strong Bioactive Glass-Based Hybrid Implants with Good Biomineralization Activity Used to Reduce Formation Duration and Improve Biomechanics of Bone Regeneration. *Polymers* **2023**, *15*, 3497. [CrossRef]
7. Scaglione, S.; Giannoni, P.; Bianchini, P.; Sandri, M.; Marotta, R.; Firpo, G.; Valbusa, U.; Tampieri, A.; Diaspro, A.; Bianco, P. Order versus disorder: In vivo bone formation within osteoconductive scaffolds. *Sci. Rep.* **2012**, *2*, 274. [CrossRef]
8. Xia, Z.; Yu, X.; Jiang, X.; Brody, H.D.; Rowe, D.W.; Wei, M. Fabrication and characterization of biomimetic collagen–apatite scaffolds with tunable structures for bone tissue engineering. *Acta Biomater.* **2013**, *9*, 7308–7319. [CrossRef]
9. Wang, Y.; Azaïs, T.; Robin, M.; Vallée, A.; Catania, C.; Legriel, P.; Pehau-Arnaudet, G.; Babonneau, F.; Giraud-Guille, M.-M.; Nassif, N. The predominant role of collagen in the nucleation, growth, structure and orientation of bone apatite. *Nat. Mater.* **2012**, *11*, 724–733. [CrossRef]
10. Zhong, C.; Chu, C.C. Biomimetic mineralization of acid polysaccharide-based hydrogels: Towards porous 3-dimensional bone-like biocomposites. *J. Mater. Chem.* **2012**, *22*, 6080–6087. [CrossRef]
11. Bal, Z.; Korkusuz, F.; Ishiguro, H.; Okada, R.; Kushioka, J.; Chijimatsu, R.; Kodama, J.; Tateiwa, D.; Ukon, Y.; Nakagawa, S. A novel nano-hydroxyapatite/synthetic polymer/bone morphogenetic protein-2 composite for efficient bone regeneration. *Spine J.* **2021**, *21*, 865–873. [CrossRef] [PubMed]
12. Correa-Piña, B.A.; Gomez-Vazquez, O.M.; Londoño-Restrepo, S.M.; Zubieta-Otero, L.F.; Millan-Malo, B.M.; Rodriguez-García, M.E. Synthesis and characterization of nano-hydroxyapatite added with magnesium obtained by wet chemical precipitation. *Prog. Nat. Sci. Mater. Int.* **2021**, *31*, 575–582. [CrossRef]

13. Londono-Restrepo, S.; Jeronimo-Cruz, R.; Millán-Malo, B.; Rivera-Munoz, E.; Rodriguez-García, M. Effect of the Nano crystal size on the X-ray diffraction patterns of biogenic hydroxyapatite from human, bovine, and porcine bones. *Sci. Rep.* **2019**, *9*, 5915. [CrossRef] [PubMed]
14. Swain, S.; Bhaskar, R.; Gupta, M.K.; Sharma, S.; Dasgupta, S.; Kumar, A.; Kumar, P. Mechanical, electrical, and biological properties of mechanochemically processed hydroxyapatite ceramics. *Nanomaterials* **2021**, *11*, 2216. [CrossRef] [PubMed]
15. Kim, H.-M.; Himeno, T.; Kokubo, T.; Nakamura, T. Process and kinetics of bonelike apatite formation on sintered hydroxyapatite in a simulated body fluid. *Biomaterials* **2005**, *26*, 4366–4373. [CrossRef]
16. Abe, Y.; Kokubo, T.; Yamamuro, T. Apatite coating on ceramics, metals and polymers utilizing a biological process. *J. Mater. Sci. Mater. Med.* **1990**, *1*, 233–238. [CrossRef]
17. Weng, J.; Liu, Q.; Wolke, J.; Zhang, X.; De Groot, K. Formation and characteristics of the apatite layer on plasma-sprayed hydroxyapatite coatings in simulated body fluid. *Biomaterials* **1997**, *18*, 1027–1035. [CrossRef]
18. Zhang, L.-J.; Feng, X.-S.; Liu, H.-G.; Qian, D.-J.; Zhang, L.; Yu, X.-L.; Cui, F.-Z. Hydroxyapatite/collagen composite materials formation in simulated body fluid environment. *Mater. Lett.* **2004**, *58*, 719–722. [CrossRef]
19. Lindberg, F.; Heinrichs, J.; Ericson, F.; Thomsen, P.; Engqvist, H. Hydroxylapatite growth on single-crystal rutile substrates. *Biomaterials* **2008**, *29*, 3317–3323. [CrossRef]
20. Georgeanu, V.A.; Gingu, O.; Antoniac, I.V.; Manolea, H.O. Current Options and Future Perspectives on Bone Graft and Biomaterials Substitutes for Bone Repair, from Clinical Needs to Advanced Biomaterials Research. *Appl. Sci.* **2023**, *13*, 8471. [CrossRef]
21. Petite, H.; Viateau, V.; Bensaid, W.; Meunier, A.; de Pollak, C.; Bourguignon, M.; Oudina, K.; Sedel, L.; Guillemin, G. Tissue-engineered bone regeneration. *Nat. Biotechnol.* **2000**, *18*, 959–963. [CrossRef] [PubMed]
22. Cesarano, J., III; Dellinger, J.G.; Saavedra, M.P.; Gill, D.D.; Jamison, R.D.; Grosser, B.A.; Sinn-Hanlon, J.M.; Goldwasser, M.S. Customization of load-bearing hydroxyapatite lattice scaffolds. *Int. J. Appl. Ceram. Technol.* **2005**, *2*, 212–220. [CrossRef]
23. Hulbert, S.; Young, F.; Mathews, R.; Klawitter, J.; Talbert, C.; Stelling, F. Potential of ceramic materials as permanently implantable skeletal prostheses. *J. Biomed. Mater. Res.* **1970**, *4*, 433–456. [CrossRef]
24. Guillemin, G.; Meunier, A.; Dallant, P.; Christel, P.; Pouliquen, J.C.; Sedel, L. Comparison of coral resorption and bone apposition with two natural corals of different porosities. *J. Biomed. Mater. Res.* **1989**, *23*, 765–779. [CrossRef] [PubMed]
25. Dinescu, S.; Ionita, M.; Ignat, S.-R.; Costache, M.; Hermenean, A. Graphene oxide enhances chitosan-based 3D scaffold properties for bone tissue engineering. *Int. J. Mol. Sci.* **2019**, *20*, 5077. [CrossRef]
26. Chatzipetros, E.; Christopoulos, P.; Donta, C.; Tosios, K.I.; Tsiambas, E.; Tsiourvas, D.; Kalogirou, E.-M.; Tsiklakis, K. Application of nano-hydroxyapatite/chitosan scaffolds on rat calvarial critical-sized defects: A pilot study. *Med. Oral Patol. Oral Cir. Bucal* **2018**, *23*, e625. [CrossRef]
27. Chatzipetros, E.; Yfanti, Z.; Christopoulos, P.; Donta, C.; Damaskos, S.; Tsiambas, E.; Tsiourvas, D.; Kalogirou, E.-M.; Tosios, K.I.; Tsiklakis, K. Imaging of nano-hydroxyapatite/chitosan scaffolds using a cone beam computed tomography device on rat calvarial defects with histological verification. *Clin. Oral Investig.* **2020**, *24*, 437–446. [CrossRef]
28. Dey, A.; Bomans, P.H.; Müller, F.A.; Will, J.; Frederik, P.M.; de With, G.; Sommerdijk, N.A. The role of prenucleation clusters in surface-induced calcium phosphate crystallization. *Nat. Mater.* **2010**, *9*, 1010–1014. [CrossRef]
29. Cölfen, H. A crystal-clear view. *Nat. Mater.* **2010**, *9*, 960–961. [CrossRef]
30. Liang, H.; Mirinejad, M.S.; Asefnejad, A.; Baharifar, H.; Li, X.; Saber-Samandari, S.; Toghraie, D.; Khandan, A. Fabrication of tragacanthin gum-carboxymethyl chitosan bio-nanocomposite wound dressing with silver-titanium nanoparticles using freeze-drying method. *Mater. Chem. Phys.* **2022**, *279*, 125770. [CrossRef]
31. Khan, M.U.A.; Al-Thebaiti, M.A.; Hashmi, M.U.; Aftab, S.; Abd Razak, S.I.; Abu Hassan, S.; Abdul Kadir, M.R.; Amin, R. Synthesis of silver-coated bioactive nanocomposite scaffolds based on grafted beta-glucan/hydroxyapatite via freeze-drying method: Anti-microbial and biocompatibility evaluation for bone tissue engineering. *Materials* **2020**, *13*, 971. [CrossRef] [PubMed]
32. Kardan-Halvaei, M.; Morovvati, M.; Angili, S.N.; Saber-Samandari, S.; Razmjooee, K.; Toghraie, D.; Khandan, A. Fabrication of 3D-printed hydroxyapatite using freeze-drying method for bone regeneration: RVE and finite element simulation analysis. *J. Mater. Res. Technol.* **2023**, *24*, 8682–8692. [CrossRef]
33. Kim, H.-M.; Kim, Y.; Park, S.-J.; Rey, C.; Lee, H.; Glimcher, M.J.; Ko, J.S. Thin film of low-crystalline calcium phosphate apatite formed at low temperature. *Biomaterials* **2000**, *21*, 1129–1134. [CrossRef] [PubMed]
34. Hernandez-Toledano, D.S.; Salazar-Osorio, A.I.; Medina-Buelvas, D.M.; Romero-Martínez, J.; Estrada-Muñiz, E.; Vega, L. Methylated and ethylated dialkylphosphate metabolites of organophosphate pesticides: DNA damage in bone marrow cells of Balb/c mice. *Mutat. Res. Genet. Toxicol. Environ. Mutagen.* **2023**, *889*, 503641. [CrossRef]
35. Wang, Z.; Mi, F.; Li, J.; Chen, D.; Lin, M.; Wang, X.; Wu, S.; Wu, C.; Liu, C. Bone Marrow Stromal Cells Sorted by Semiconducting Polymer Nanodots for Bone Repair. *ACS Biomater. Sci. Eng.* **2023**, *9*, 5772–5781. [CrossRef]
36. Shao, C.; Liu, Y.; Li, J.; Liu, Z.; Zhao, Y.; Jing, Y.; Lv, Z.; Fu, T.; Wang, Z.; Li, G. Up-regulated IL-17 and Tnf signaling in bone marrow cells of young male osteogenesis imperfecta mice. *PeerJ* **2022**, *10*, e13963. [CrossRef]
37. Ducheyne, P.; Mauck, R.L.; Smith, D.H. Biomaterials in the repair of sports injuries. *Nat. Mater.* **2012**, *11*, 652–654. [CrossRef]
38. Ielo, I.; Calabrese, G.; De Luca, G.; Conoci, S. Recent advances in hydroxyapatite-based biocomposites for bone tissue regeneration in orthopedics. *Int. J. Mol. Sci.* **2022**, *23*, 9721. [CrossRef]

39. Uppal, G.; Thakur, A.; Chauhan, A.; Bala, S. Magnesium based implants for functional bone tissue regeneration–A review. *J. Magnes. Alloys* **2022**, *10*, 356–386. [CrossRef]
40. Pupilli, F.; Ruffini, A.; Dapporto, M.; Tavoni, M.; Tampieri, A.; Sprio, S. Design strategies and biomimetic approaches for calcium phosphate scaffolds in bone tissue regeneration. *Biomimetics* **2022**, *7*, 112. [CrossRef]
41. Khvorostina, M.A.; Mironov, A.V.; Nedorubova, I.A.; Bukharova, T.B.; Vasilyev, A.V.; Goldshtein, D.V.; Komlev, V.S.; Popov, V.K. 3D Printed Gene-Activated Sodium Alginate Hydrogel Scaffolds. *Gels* **2022**, *8*, 421. [CrossRef] [PubMed]
42. Nedorubova, I.A.; Bukharova, T.B.; Mokrousova, V.O.; Khvorostina, M.A.; Vasilyev, A.V.; Nedorubov, A.A.; Grigoriev, T.E.; Zagoskin, Y.D.; Chvalun, S.N.; Kutsev, S.I. Comparative Efficiency of Gene-Activated Matrices Based on Chitosan Hydrogel and PRP Impregnated with BMP2 Polyplexes for Bone Regeneration. *Int. J. Mol. Sci.* **2022**, *23*, 14720. [CrossRef] [PubMed]
43. Khvorostina, M.; Mironov, A.; Nedorubova, I.; Bukharova, T.; Vasilyev, A.; Goldshtein, D.; Komlev, V.; Popov, V. Osteogenesis Enhancement with 3D Printed Gene-Activated Sodium Alginate Scaffolds. *Gels* **2023**, *9*, 315. [CrossRef] [PubMed]
44. Power, R.N.; Cavanagh, B.L.; Dixon, J.E.; Curtin, C.M.; O'Brien, F.J. Development of a Gene-Activated Scaffold Incorporating Multifunctional Cell-Penetrating Peptides for pSDF-1α Delivery for Enhanced Angiogenesis in Tissue Engineering Applications. *Int. J. Mol. Sci.* **2022**, *23*, 1460. [CrossRef] [PubMed]
45. Al-Munajjed, A.A.; Plunkett, N.A.; Gleeson, J.P.; Weber, T.; Jungreuthmayer, C.; Levingstone, T.; Hammer, J.; O'Brien, F.J. Development of a biomimetic collagen-hydroxyapatite scaffold for bone tissue engineering using a SBF immersion technique. *J. Biomed. Mater. Res. Part B Appl. Biomater.* **2009**, *90*, 584–591. [CrossRef] [PubMed]
46. Diao, Y.; Harada, T.; Myerson, A.S.; Alan Hatton, T.; Trout, B.L. The role of nanopore shape in surface-induced crystallization. *Nat. Mater.* **2011**, *10*, 867–871. [CrossRef]
47. De Yoreo, J. More than one pathway. *Nat. Mater.* **2013**, *12*, 284–285. [CrossRef]
48. Desiraju, G.R. Crystal engineering: From molecule to crystal. *J. Am. Chem. Soc.* **2013**, *135*, 9952–9967. [CrossRef]
49. Bianchi, E.; Vigani, B.; Viseras, C.; Ferrari, F.; Rossi, S.; Sandri, G. Inorganic nanomaterials in tissue engineering. *Pharmaceutics* **2022**, *14*, 1127. [CrossRef]
50. Xue, N.; Ding, X.; Huang, R.; Jiang, R.; Huang, H.; Pan, X.; Min, W.; Chen, J.; Duan, J.-A.; Liu, P. Bone tissue engineering in the treatment of bone defects. *Pharmaceuticals* **2022**, *15*, 879. [CrossRef]
51. Ressler, A. Chitosan-Based Biomaterials for Bone Tissue Engineering Applications: A Short Review. *Polymers* **2022**, *14*, 3430. [CrossRef] [PubMed]
52. Fatimi, A.; Okoro, O.V.; Podstawczyk, D.; Siminska-Stanny, J.; Shavandi, A. Natural hydrogel-based bio-inks for 3D bioprinting in tissue engineering: A review. *Gels* **2022**, *8*, 179. [CrossRef] [PubMed]
53. Yazdanpanah, Z.; Johnston, J.D.; Cooper, D.M.; Chen, X. 3D bioprinted scaffolds for bone tissue engineering: State-of-the-art and emerging technologies. *Front. Bioeng. Biotechnol.* **2022**, *10*, 824156. [CrossRef] [PubMed]
54. Harish, V.; Tewari, D.; Gaur, M.; Yadav, A.B.; Swaroop, S.; Bechelany, M.; Barhoum, A. Review on nanoparticles and nanostructured materials: Bioimaging, biosensing, drug delivery, tissue engineering, antimicrobial, and agro-food applications. *Nanomaterials* **2022**, *12*, 457. [CrossRef] [PubMed]